Exp.-Nr. **A2-11/09**
Eingang: 15.05.2009
an PAC: 18.05.2009

Mainz Microtron MAMI

Collaboration A2: "Tagged Photons"
Spokesperson: A. Thomas

Proposal for an Experiment

"Measurement of the Proton Spin Polarizabilities"

Spokespersons for the Experiment :

D. Hornidge (Mount Allison)
E.J. Downie (Mainz)
J.R.M. Annand (Glasgow)
I.J.D. MacGregor (Glasgow)

Abstract of Physics :

We propose to perform three precise Compton scattering experiments to extract the spin polarizabilities of the proton. These four structure constants are fundamental observables describing the spin response of the nucleon, and they have generated considerable theoretical interest in recent years. Using subtracted dispersion relations, the values of the known static polarizabilities, α_{E1} and β_{M1}, and a measurement of one beam and two beam-target asymmetries, we intend to extract all four quantities.

Abstract of Equipment :

The experiment will be performed at the tagged photon facility of MAMI using polarized photon beams (both linear and circular) from the Glasgow tagger incident on both polarized (butanol) and unpolarized (liquid hydrogen) targets, with the reaction products being detected using the CB-TAPS system.

MAMI Specifications :

beam energy	1508 MeV and 380 MeV
beam current	< 100 nA
beam polarisation	polarized and unpolarized

Photon Beam Specifications :

tagged energy range	200–1402 MeV and 200–353 MeV
photon beam polarisation	linear and circular

Equipment Specifications :

detectors	Crystal Ball/TAPS
target	frozen-spin butanol (both longitudinal and transverse polarization) and 5-cm LH_2

Beam Time Request :

set–up/tests with beam	36 hours (12 per measurement)
data taking	780 hours (340 in parallel with A2/10-09)

List of participating authors:

Institut für Physik, University of Basel, Switzerland
I. Jaegle, I. Keshelashvili, B. Krusche, Y. Maghrbi, F. Pheron, T. Rostomyan, D. Werthmüller

Institut für Experimentalphysik, University of Bochum, Germany
W. Meyer, G. Reicherz

Helmholtz–Institut für Strahlen- und Kernphysik, University of Bonn, Germany
R. Beck, A. Nikolaev

Massachusetts Institute of Technology , Cambridge, USA
A. Bernstein, W. Deconinck

JINR, Dubna, Russia
N. Borisov, A. Lazarev, A. Neganov, Yu.A. Usov

School of Physics, University of Edinburgh, UK
D. Branford, D.I. Glazier, T. Jude, M. Sikora, D.P. Watts

Petersburg Nuclear Physics Institute, Gatchina, Russia
V. Bekrenev, S. Kruglov, A. Koulbardis

Department of Physics and Astronomy, University of Glasgow, UK
J.R.M. Annand, D. Hamilton, D. Howdle, K. Livingston, J. Mancell, J.C. McGeorge, I.J.D. MacGregor, E.F. McNicoll, R.O. Owens, J. Robinson, G. Rosner

Department of Astronomy and Physics, Saint Mary's University Halifax, Canada
A.J. Sarty

Kent State University, Kent, USA
D.M. Manley

University of California, Los Angeles, USA
B.M.K. Nefkens, S. Prakhov, A. Starostin, I.M. Suarez

MAX-lab, University of Lund, Sweden
L. Isaksson

Institut für Kernphysik, University of Mainz, Germany
P. Aguar-Bartolome, H.J. Arends, S. Bender, A. Denig, E.J. Downie, N. Frömmgen, E. Heid, O. Jahn, H. Ortega, M. Ostrick, B.Oussena, P.B. Otte, S. Schumann, A. Thomas, M. Unverzagt

Institut für Physik, University of Mainz, D
J. Krimmer, W. Heil

University of Massachusetts, Amherst, USA
P. Martel, R. Miskimen

Institute for Nuclear Research, Moscow, Russia
G. Gurevic, R. Kondratiev, V. Lisin, A. Polonski

Lebedev Physical Institute, Moscow, Russia
S.N. Cherepnya, L.V. Fil kov, V.L. Kashevarov

INFN Sezione di Pavia, Pavia, Italy
A. Braghieri, A. Mushkarenkov, P. Pedroni

Department of Physics, University of Regina, Canada
G.M. Huber

Mount Allison University, Sackville, Canada
D. Hornidge

Tomsk Polytechnic University, Tomsk, Russia
A. Fix

Physikalisches Institut, University of Tübingen, Germany
P. Grabmayr, T. Hehl, D.G. Middleton

George Washington University, Washington, USA
W. Briscoe, T. Morrison, B. Oussena, B. Taddesse, M. Taragin

Catholic University, Washington, USA
D. Sober

Rudjer Boskovic Institute, Zagreb, Croatia
M. Korolija, D. Mekterovic, S. Micanovic, I. Supek

1 Motivation

Nucleon polarizabilities are fundamental structure observables like the charge and mass, but are related to the nucleon's internal dynamics—making them ideally suited for constraining/testing QCD-based models of nucleon structure. Although the two scalar (spin-independent) polarizabilities, α_{E1} and β_{M1}, are well understood for the proton, very few experiments have attempted to extract the spin polarizabilities—which can be written as γ_{E1E1}, γ_{M1M1}, γ_{M1E2}, and γ_{E1M2}—and none have managed to separate all four. There are two combinations that have been measured:

$$\gamma_0 = -\gamma_{E1E1} - \gamma_{M1M1} - \gamma_{E1M2} - \gamma_{M1E2}$$

which is known as the forward spin polarizability, and

$$\gamma_\pi = -\gamma_{E1E1} + \gamma_{M1M1} - \gamma_{E1M2} + \gamma_{M1E2},$$

which is known as the backward spin polarizability, and they have errors on the order of 10% and 25%, respectively (see Table 1).

Unlike the scalar polarizabilities, where α_{E1} can be thought of as the electric "stretchability" and β_{M1} the magnetic "alignability", these higher order polarizabilities unfortunately have no classical analog, but can be thought of as parametrizing the "stiffness" of the nucleon against electromagnetically induced deformations relative to the nucleon spin axis [1]. The scalar polarizabilities appear in the effective interaction Hamiltonian at second order in photon energy

$$H_{\text{eff}}^{(2)} = -4\pi \left[\tfrac{1}{2}\alpha_{E1}\vec{E}^2 + \tfrac{1}{2}\beta_{M1}\vec{H}^2 \right]$$

and describe the response of the nucleon's internal structure to an external electric or magnetic field, whereas the spin polarizabilities enter at third order:

$$H_{\text{eff}}^{(3)} = -4\pi \Big[\tfrac{1}{2}\gamma_{E1E1}\vec{\sigma}\cdot(\vec{E}\times\dot{\vec{E}}) + \tfrac{1}{2}\gamma_{M1M1}\vec{\sigma}\cdot(\vec{H}\times\dot{\vec{H}}) - \gamma_{M1E2}E_{ij}\sigma_i H_j + \gamma_{E1M2}H_{ij}\sigma_i E_j \Big] .$$

There has been much recent theoretical interest in extracting these quantities, using both chiral effective field theory and subtracted dispersion relations [1, 2, 3, 4, 5, 6, 7, 8, 9, 10, 11], and lattice calculations are currently underway [12]. At the recent MAMI and Beyond Conference, talks by Holstein, Miskimen, and Pasquini spoke at length about the importance of new measurements to determine the four spin polarizabilities, which are yet unknown fundamental properties of the nucleon. Precise polarized real Compton scattering experiments are required to identify these four spin polarizabilities individually because of contributions from the larger anomaly (pion pole) contribution. Despite the technical challenge these experiments pose, these speakers emphasized that this measurement should be an important goal for laboratories such as MAMI, with B. Holstein listing it as his number one priority in his summary talk for Precision Physics at the 1 GeV Scale.

Theoretical predictions together with experimental values of the forward [13] and backward [14] combinations are given in Table 1.

1.1 Asymmetries

The spin polarizabilities of the proton can be extracted by measuring various beam and beam-target asymmetries. Following the notation given in [2], we can write down the following three asymmetries that are relevant to this proposal:

1. Linearly polarized photons, either parallel or perpendicular to the scattering plane, with an unpolarized target (commonly known as the beam asymmetry):

$$\Sigma_3 = \frac{\sigma^{\parallel} - \sigma^{\perp}}{\sigma^{\parallel} + \sigma^{\perp}}$$

Table 1: Proton spin polarizability predictions and measurements in units of $10^{-4}\,\mathrm{fm}^4$. The first two predictions are from ChPT, the third is a Lorentz invariant ChPT calculation, SSE is a small scale expansion, and the remaining four are from dispersion theory. The pion-pole contribution has been subtracted from the experimental γ_π.

γ	Theory								Experiment
	$\mathcal{O}(p^4)$[7]	$\mathcal{O}(p^5)$[8]	LC4[9]	SSE[3]	BGLMN[6]	HDPV[10]	KS[11]	DPV[2,4]	
$E1E1$	−1.4	−1.8	−2.8	−5.7	−3.4	−4.3	−5.0	−4.3	no data
$M1M1$	3.3	2.9	−3.1	3.1	2.7	2.9	3.4	2.9	no data
$E1M2$	0.2	0.7	0.8	0.98	0.3	−0.01	−1.8	0	no data
$M1E2$	1.8	1.8	0.3	0.98	1.9	2.1	1.1	2.1	no data
0	3.9	−3.6	4.8	0.64	−1.5	−0.7	2.3	−0.7	$-1.01 \pm 0.08 \pm 0.13$[13]
π	6.3	5.8	−0.8	8.8	7.7	9.3	11.3	9.3	8.0 ± 1.8[14]

2. Circular photon polarization (either right-handed, R, or left-handed, L) and target spin aligned longitudinally ($\pm z$) w.r.t. the incident beam direction:

$$\Sigma_{2z} = \frac{\sigma^R_{+z} - \sigma^L_{+z}}{\sigma^R_{+z} + \sigma^L_{+z}} = \frac{\sigma^R_{+z} - \sigma^R_{-z}}{\sigma^R_{+z} + \sigma^R_{-z}}$$

3. Circular photon polarization (either right-handed, R, or left-handed, L) and target spin aligned transversely ($\pm x$) w.r.t. the incident beam direction:

$$\Sigma_{2x} = \frac{\sigma^R_{+x} - \sigma^L_{+x}}{\sigma^R_{+x} + \sigma^L_{+x}} = \frac{\sigma^R_{+x} - \sigma^R_{-x}}{\sigma^R_{+x} + \sigma^R_{-x}}$$

2 Experiment

The best way to extract the spin polarizabilities of the proton is to measure Compton scattering on the proton with polarization degrees of freedom. Using subtracted dispersion relations [2, 4], the static polarizabilities, α_{E1} and β_{M1}, the linear combinations γ_0 and γ_π, and polarized beams and targets, one can extract all four. However, it is also possible to conduct a more complex analysis and independently extract all four polarizabilities without the values of γ_0 and γ_π.

Due to the appearance of the spin polarizabilities in the effective interaction Hamiltonian at third order in photon energy, it is in the resonance region where their effect becomes significant. In the range $E_\gamma = 200 - 300$ MeV, it is possible to accurately determine a number of asymmetries from which the spin polarizabilities can be then extracted. Throughout, we use the notation of [2] where the asymmetries are given by the Stokes parameters.

We propose to conduct three separate experiments with configurations:

1. a measurement of the beam asymmetry Σ_3 using linearly polarized photons with an unpolarized liquid-hydrogen target,

2. a measurement of the beam-target asymmetry Σ_{2z} using circularly polarized photons and a longitudinally polarized target, and

3. a measurement of the beam-target asymmetry Σ_{2x} using circularly polarized photons and a transversely polarized target.

In principle, a relatively simple analysis of two of these measurements along with γ_0 and γ_π would be enough to give an accurate extraction of the four spin polarizabilities, but if we do all three, it should be possible to extract all four *independently* with very small statistical *and* systematic errors. This powerful technique takes advantage of the different effects the individual spin polarizabilities have on the energy and angular dependencies of the asymmetries [15]. A projection of the resulting uncertainties in the spin polarizabilities

when they are extracted independently requires a detailed analysis that is not yet finished. The authors expect this study to be completed in time for the oral presentation in June, and will submit to the PAC a supplemental report on them at that time.

Plots of the three asymmetries given above are shown in Figures 1, 2, and 3 along with expected experimental error bars for the conditions described in Section 3.

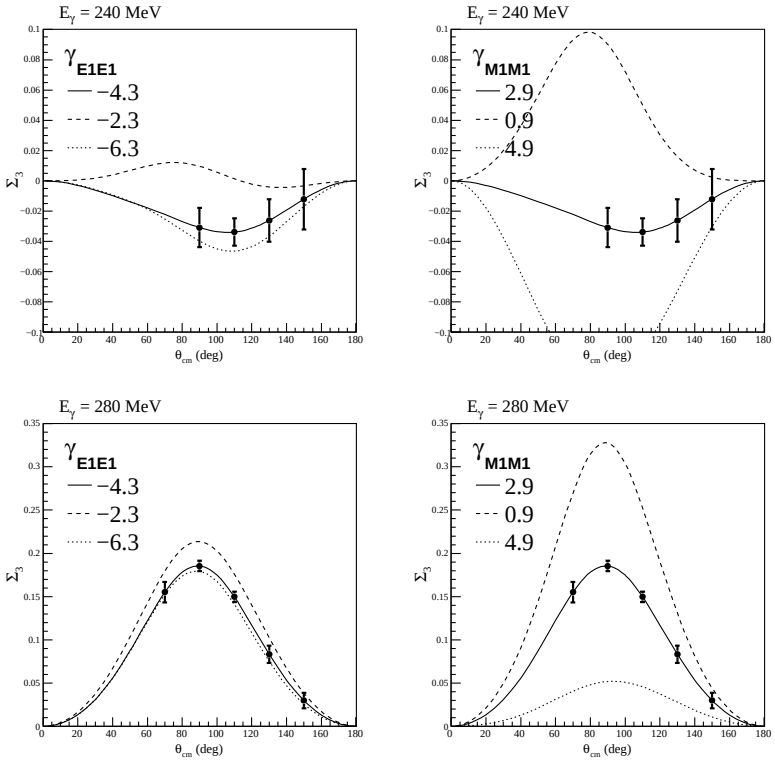

Figure 1: The beam asymmetry Σ_3 is shown as a function of scattered photon angle for $E_\gamma = 240\,\text{MeV}$ (top row) and $E_\gamma = 280\,\text{MeV}$ (bottom row). Curves are the dispersion calculation DPV [2, 4] from Table 1. In all four plots γ_{E1M2} and γ_{M1E2} are held constant, while in the left column γ_{M1M1} is fixed and γ_{E1E1} is varied, and the right column the converse is true. One can see that Σ_3 is more sensitive to changes in γ_{M1M1}, and the relative insensitivity w.r.t. γ_{E1E1} increases with increasing incident photon energy. The points show the angles at which measurements will be made and expected errors for 100 hours running.

2.1 Background Reactions

The measurement of Compton scattering in the resonance region is made difficult due to its low cross section compared to competing background reactions.

In a measurement of the beam asymmetry using an unpolarized liquid-hydrogen target, the overwhelming source of background is π^0 production from the proton where one of the two decay photons goes undetected. For measurements with the frozen-spin target, which contains oxygen and carbon in addition to hydrogen, one also needs to consider coherent Compton scattering and π^0 production from the heavier nuclei along with quasi-free (QF) processes where the photon or π^0 is produced on a proton inside the nucleus and the proton is subsequently knocked out.

Because the Crystal Ball and TAPS detector system covers very nearly 4π, the contribution from π^0 production where one photon escapes is suppressed dramatically. Moreover, if one requires the detection of the proton, contributions from the coherent reactions on carbon and oxygen vanish because there is no proton in the final state, and one has more kinematical information to help eliminate background. Specifically, one can calculate and cut on the opening angle, θ_{open}, which is the difference in angle between the measured proton momentum and that calculated from the scattered photon kinematics. Cutting on target missing mass assuming the reaction occurs on a proton, in addition to cutting on the opening angle, we can eliminate

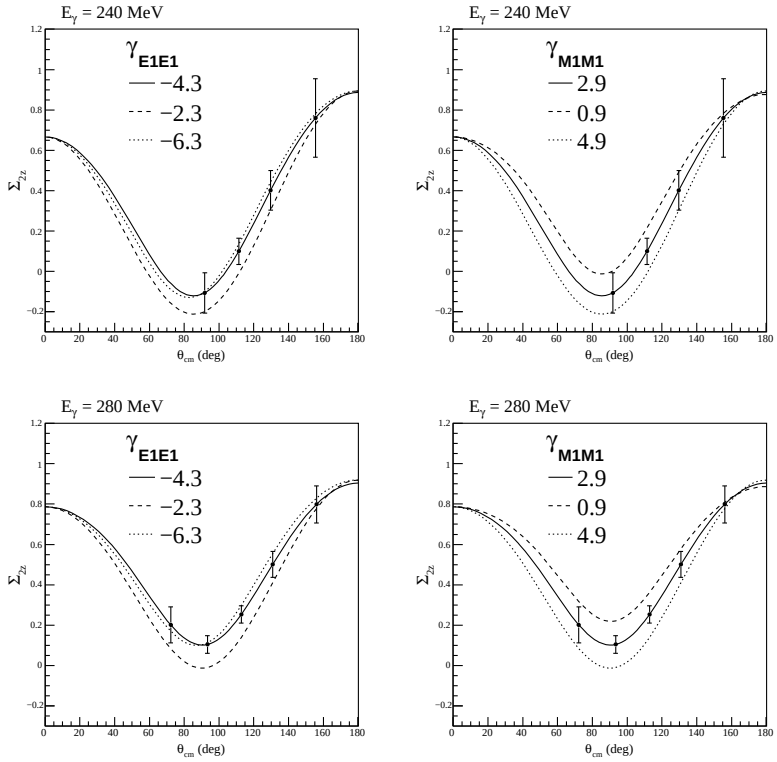

Figure 2: The beam-target asymmetry Σ_{2z} is shown as a function of scattered photon angle for $E_\gamma = 240\,\text{MeV}$ (top row) and $E_\gamma = 280\,\text{MeV}$ (bottom row). Curves are the dispersion calculation DPV [2, 4] from Table 1. In all four plots γ_{E1M2} and γ_{M1E2} are held constant, while in the left column γ_{M1M1} is fixed and γ_{E1E1} is varied, and the right column the converse is true. The points show the angles at which measurements will be made and expected errors for 300 hours running.

most of the π^0 background. Because the π^0 has a finite beam asymmetry of its own, it is necessary to exclude as many of these counts as possible without significantly reducing the Compton channel. Sample missing mass histograms from a Monte Carlo simulation of the detector set-up for the hydrogen target and energies $E_\gamma = 240\,\text{MeV}$ and $E_\gamma = 280\,\text{MeV}$ are shown in Figure 4. Note that all processes have realistic angular distributions, and backgrounds are scaled according to total cross sections.

As mentioned above, because of the butanol ($C_4H_{10}O$) in the frozen-spin target, the QF processes pose a problem, but because the protons from QF production are not polarized, they do not contribute to the beam-target asymmetry directly but rather dilute it. The magnitude of this effect is given below in (3). Simulated missing mass spectra for the frozen-spin target are shown in Figure 5.

It should be pointed out that in the analysis of simulated data, only the recoil proton angle was used, and not its energy. Including this additional information coupled with kinematic fitting should both increase the detection efficiency for the proton Compton channel and reduce the effective dilution factor from background contributions.

3 Event Rates and Uncertainties

The event rate for a specific E_γ and $\theta_{\gamma'}$ bin is given by:

$$\dot{N}_{\gamma' p} = \varepsilon_{\text{tag}}\ \dot{N}_e\ \frac{d\sigma}{d\Omega}\ t\ \varepsilon_{\gamma' p}\ \Delta\Omega\ \varepsilon_{\text{DA}} \tag{1}$$

where ε_{tag} is the tagging efficiency, $\dot{N}_e$ is the tagged electron flux, $d\sigma/d\Omega$ is the differential cross section for Compton scattering, t is the number of target nuclei per area including filling factor, $\varepsilon_{\gamma' p}$ is the detection efficiency for the scattered photon and recoil proton, $\Delta\Omega$ is the solid angle of the bin, and ε_{DA} is the data-acquisition live time.

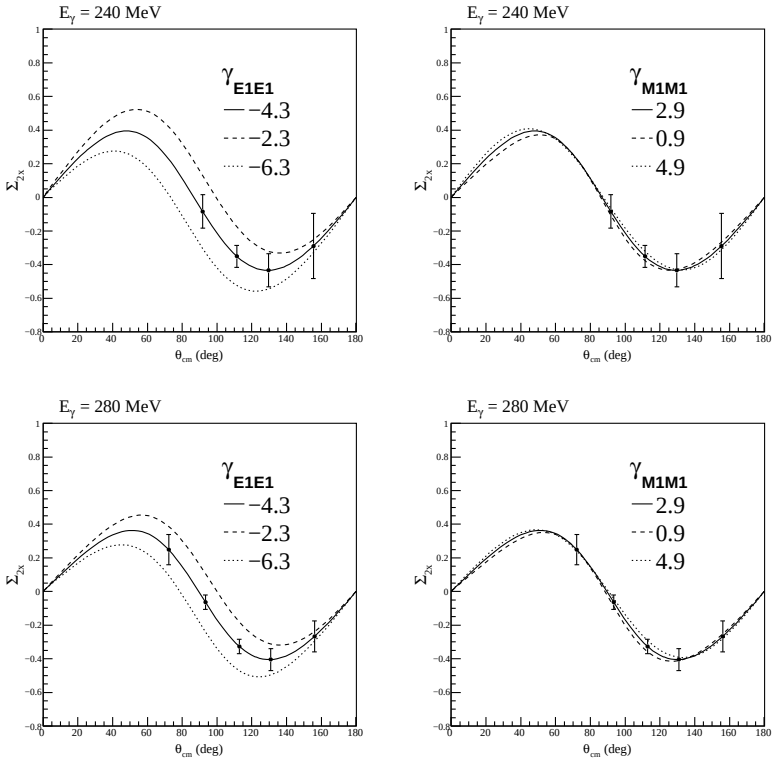

Figure 3: The beam-target asymmetry Σ_{2x} is shown as a function of scattered photon angle for $E_\gamma = 240\,\mathrm{MeV}$ (top row) and $E_\gamma = 280\,\mathrm{MeV}$ (bottom row). Curves are the dispersion calculation DPV [2, 4] from Table 1. In all four plots γ_{E1M2} and γ_{M1E2} are held constant, while in the left column γ_{M1M1} is fixed and γ_{E1E1} is varied, and the right column the converse is true. One can see that Σ_{2x} is sensitive only to changes in γ_{E1E1} regardless of incident photon energy. The points show the angles at which measurements will be made and expected errors for 300 hours running.

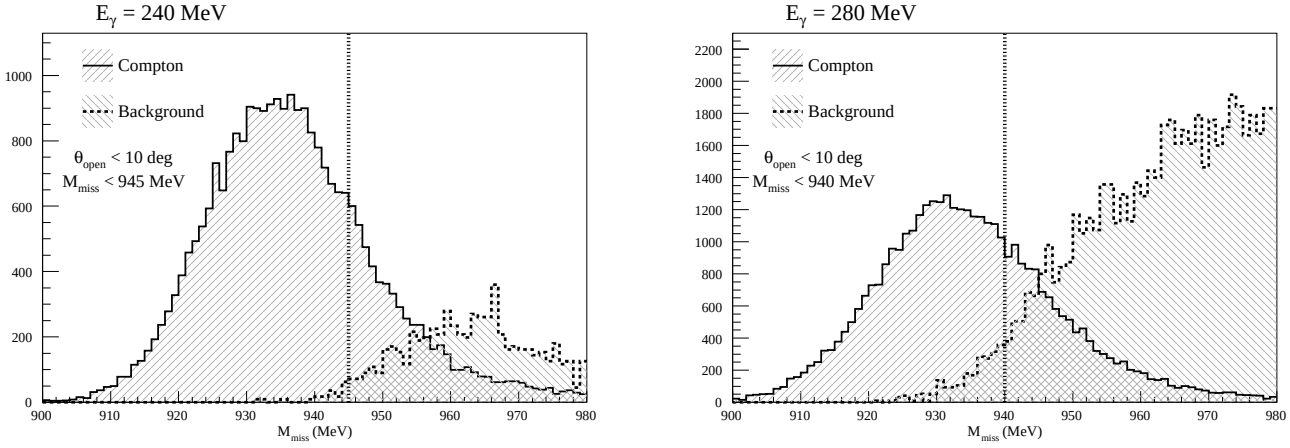

Figure 4: Simulated missing mass spectra for the hydrogen target and energies $E_\gamma = 240\,\mathrm{MeV}$ (left) and $E_\gamma = 280\,\mathrm{MeV}$ (right). Shown are the proton Compton channel, the π^0 background contribution, and the cuts used.

To calculate the error in an asymmetry with both polarized beam and polarized target, we use

$$\delta\Sigma \simeq \frac{1}{p_\gamma\, p_T} \frac{1}{\sqrt{2N_{\gamma' p}\, D_{\mathrm{eff}}}} \tag{2}$$

where p_γ is the degree of beam polarization, p_T is the target polarization, and D_{eff} is the effective dilution

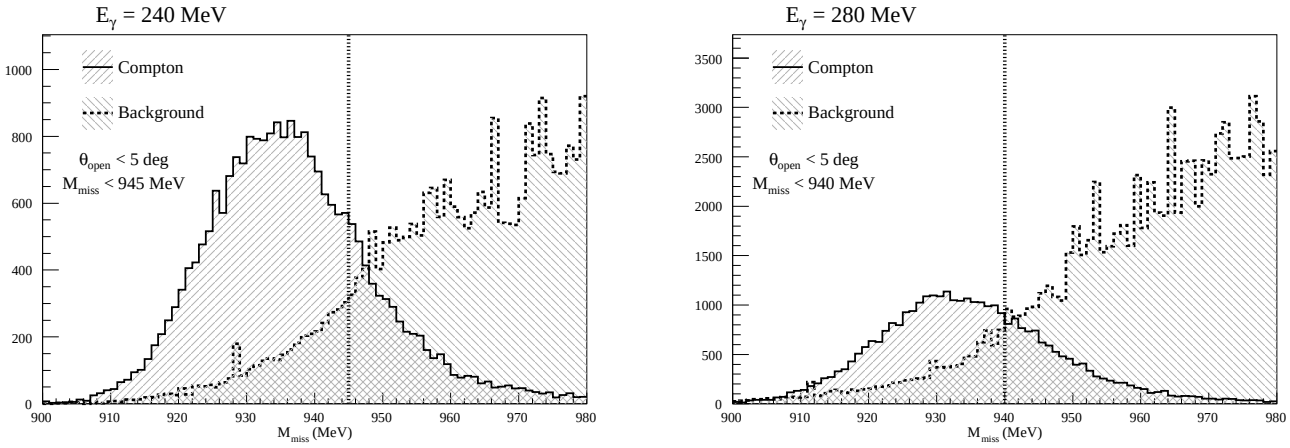

Figure 5: Simulated missing mass histograms for the frozen-spin target and energies $E_\gamma = 240\,\mathrm{MeV}$ (left) and $E_\gamma = 280\,\mathrm{MeV}$ (right). The processes contributing to the background are π^0 production from the free proton, QF π^0 production and QF Compton scattering from the carbon and oxygen in butanol.

factor from the competing background reactions given by

$$D_{\mathrm{eff}} = \frac{N_{\gamma' p}}{N_{\gamma' p} + N_{\mathrm{background}}}. \tag{3}$$

For an unpolarized target, the factors p_T and D_{eff} are unity.

In order to find the time, T, required to obtain a specific uncertainty, we replace $N_{\gamma' p}$ in (2) with $\dot{N}_{\gamma' p} T$ and then rearrange:

$$T = \left[(\delta\Sigma\, p_\gamma\, p_T)^2 2 \dot{N}_{\gamma' p} D_{\mathrm{eff}} \right]^{-1}$$

where again, for an unpolarized target p_T and D_{eff} are one.

The following parameters are common to all three of the measurements:

- Photon energy region of interest: $E_\gamma = 200 - 300$ MeV.
- Data acquisition live time: $\varepsilon_{DA} \approx 0.7$.
- The solid angle for a specific θ-bin is given by the standard formula:

$$\Delta\Omega(\theta) = \int_0^{2\pi} d\phi \int_{\theta_1}^{\theta_2} \sin\theta d\theta,$$

  where here we have integrated over ϕ and $\Delta\theta = 20^\circ$.

Due the necessity of requiring a proton in coincidence with the scattered photon for background elimination, it is not possible to make use of the full angular range afforded by the CB-TAPS setup. The minimum proton momentum that can be detected is expected to be roughly 280 MeV/c, reducing the detection efficiency for forward-scattered photons. This is evident in Tables 2 and 3.

3.1 Linearly Polarized Photons, Unpolarized Target

The parameters entering the count-rate estimate and resulting beam-time request for the linearly polarized beam and an unpolarized liquid-hydrogen target are:

- Incoming electron beam energy: $E_0 = 1508$ MeV. This high value is chosen to maximize the degree of linear polarization of the photon beam in the region of interest.
- Electron count rate over region of interest: $\dot{N}_e = 175 - 260 \times 10^3\ \frac{1}{s}\ \frac{1}{\mathrm{MeV}}$.

- Tagging efficiency: $\varepsilon_{tag} \approx 0.7$.
- Number of protons in a 5-cm liquid-hydrogen target: $t = 2.0 \times 10^{23}\ \frac{1}{\mathrm{cm}^2}$.
- Degree of linear polarization over region of interest: $p_\gamma = 0.5 - 0.8$.

Tagger channels below about 200 MeV will be switched off so that photon flux can be maximized in the region of interest.

The results for incident photon energy bins $E_\gamma = 240 \pm 10$ MeV and $E_\gamma = 280 \pm 10$ MeV are given in Table 2. The detection efficiency "dip" at 130 degrees 280 MeV is due to the gap region between the Crystal

Table 2: Rate estimates and uncertainties for linearly polarized beam on an unpolarized liquid-hydrogen target as a function of scattered photon angle for $E_\gamma = 240 \pm 10$ MeV and $E_\gamma = 280 \pm 10$ MeV. Cross sections are from subtracted dispersion relations [16]. Efficiencies are obtained using a Monte Carlo simulation.

θ_π (deg)	$\Delta\Omega$ (sr)	$\varepsilon_{\gamma' p}$	$d\sigma/d\Omega$ (μb/sr)	$\dot{N}_{\gamma' p}$ (1/h/20 MeV)	$\delta\Sigma$ for 100 hours
$E_\gamma = 240$ MeV					
90	2.2	0.31	59	31	0.019
110	2.0	0.60	68	66	0.013
130	1.7	0.26	81	28	0.020
150	1.1	0.17	94	14	0.028
$E_\gamma = 280$ MeV					
70	2.0	0.16	139	30	0.017
90	2.2	0.61	130	116	0.008
110	2.0	0.55	137	104	0.009
130	1.7	0.25	157	44	0.014
150	1.1	0.35	181	47	0.013

Ball and TAPS detectors.

3.2 Circularly Polarized Photons, Polarized Target

The parameters entering the count-rate estimate and resulting beam-time request specific to the circularly polarized beam are:

- Incoming electron beam energy: $E_0 = 380$ MeV. This low value is chosen to maximize the degree of circular polarization of the photon beam in the region of interest.
- Electron count rate over region of interest: $\dot{N}_e = 60 - 70 \times 10^3\ \frac{1}{s}\ \frac{1}{\mathrm{MeV}}$. Note that the lower count rate here is necessary to limit the total flux over the tagged range on the butanol target to $5 \times 10^7\ \mathrm{s}^{-1}$.
- Tagging efficiency: $\varepsilon_{tag} \approx 0.25$.
- Degree of circular polarization over region of interest: $p_\gamma = 0.6 - 0.8$.
- Effective number of protons in the butanol target: $t = 9.1 \times 10^{22}\ \frac{1}{\mathrm{cm}^2}$.
- Average target polarization: $p_T \approx 0.7$.

The results for incident photon energy bins $E_\gamma = 240 \pm 10$ MeV and $E_\gamma = 280 \pm 10$ MeV are given in Table 3.

Table 3: Rate estimates and uncertainties for circularly polarized beam on a polarized frozen-spin target as a function of scattered photon angle for $E_\gamma = 240 \pm 10$ MeV and $E_\gamma = 280 \pm 10$ MeV. Cross sections are from subtracted dispersion relations [16]. Efficiencies and dilution factors are obtained with a Monte Carlo simulation.

θ_π (deg)	$\Delta\Omega$ (sr)	$\varepsilon_{\gamma' p}$	$D_{\rm eff}$	$d\sigma/d\Omega$ (μb/sr)	$\dot{N}_{\gamma' p}$ (1/h/20 MeV)	$\delta\Sigma$ for 300 hours
$E_\gamma = 240$ MeV						
90	2.2	0.25	0.90	59	1.3	0.081
110	2.0	0.53	0.85	68	3.0	0.054
130	1.7	0.24	0.75	81	1.3	0.086
150	1.1	0.17	0.73	94	0.7	0.121
$E_\gamma = 280$ MeV						
70	2.0	0.11	0.90	139	1.0	0.079
90	2.2	0.50	0.82	130	4.9	0.038
110	2.0	0.50	0.64	137	4.8	0.044
130	1.7	0.24	0.57	157	2.1	0.069
150	1.1	0.35	0.67	181	2.3	0.061

3.3 Beam-Time Request

To study the sensitivity of our projected data to the proton spin-polarizabilities, we create pseudo-data and then fit the data with the dispersion calculation of [2, 4]. In this analysis the spin-polarizabilities were fit to the Σ_{2z} asymmetry only, and the fit was constrained by the experimental errors for γ_0 and γ_π. To simplify the analysis we assume a single tagged photon energy of 275 MeV and a flux of 10^6 photon/s (approximately equivalent to one 20-MeV-wide bin). Running for 300 hours at 70% longitudinal target polarization and using standard target parameters, our preliminary projected errors for γ_{E1E1}, γ_{M1M1}, γ_{E1M2}, γ_{M1E2} and γ_π are 0.7, 0.4, 1.3, 0.7, and 0.8, respectively, in units of 10^{-4} fm^4. The projected error for γ_π alone is a two-fold improvement over the existing experimental error.

The sensitivity study for this experiment is in progress, and as a next step we will include asymmetry data on Σ_{2x} and Σ_3 in the analysis. Actual data will have a $1/E_\gamma$ energy distribution with photon polarization that decreases with decreasing tagged photon energy, and these effects must be included in our modeling. It is also important to include dilution effects in the asymmetries due to backgrounds (see Figure 5). Nevertheless, the projected asymmetry errors presented in Figures 1, 2, and 3, and the projected spin-polarizability errors presented here demonstrate that the experiment has sufficient sensitivity to test in detail the calculations contained in Table 1.

We propose three separate runs of 100 hours for Σ_3, 300 hours for Σ_{2z}, and 300 hours for Σ_{2x}. In addition, approximately 6 hours must be spent for every 48 hours of beam to re-polarize the frozen-spin target, resulting an additional ≈ 80 hours.

In summary, the total beam time requested is:

780 hours

.

A Experimental Apparatus

A.1 Photon Beam

The A2 photon beam is derived from the production of Bremsstrahlung photons during the passage of the MAMI electron beam through a thin radiator. The resulting photons can be circularly polarised, with the application of a polarised electron beam, or linearly polarised, in the case of a crystalline radiator. The degree of polarisation achieved is dependent on the energy of the incident photon beam (E_0) and the energy range of interest, but currently peaks at ∼75% for linear polarisation (Figure 6) and ∼85% for circular polarisation (Figure 7). The maximum degree of linear polarisation should be further improved by 5 to 10% by the end of 2009 when the collimation and beam monitoring systems will be optimised for MAMI-C during the installation of the Frozen Spin Target. The Glasgow Photon Tagger (Figure 8) provides energy tagging of the photons by detecting the post-radiating electrons and can determine the photon energy with a resolution of 2 to 4 MeV depending on the incident beam energy, with a single-counter time resolution $\sigma_t = 0.117$ ns [19]. Each counter can operate reliably to a rate of ∼1 MHz, giving a photon flux of $2.5 \cdot 10^5$ photons per MeV. Photons can be tagged in the momentum range from 4.7 to 93.0% of E_0.

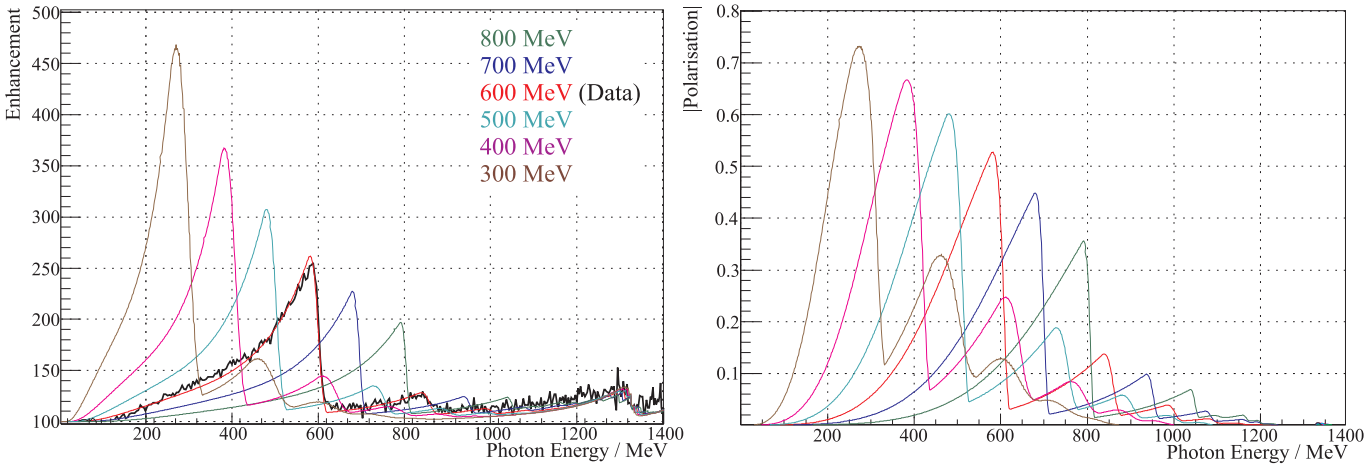

Figure 6: Linear polarisation available with the current collimation system for a variety of crystal orientations. The thin black lines are data obtained during recent MAMI-C runs.

To augment the standard focal plane detector system and make use of the Tagger's intrinsic energy resolution of 0.4 MeV (FWHM), there exists a scintillating fibre detector ('Tagger Microscope') that can improve the energy resolution by a factor of about 6 for a ∼100 MeV wide region of the focal plane (dependent on its position) [21].

A.2 Frozen-Spin Target

Polarisation experiments using high density solid-state targets in combination with tagged photon beams can reach the highest luminosities. For the double polarisation measurements planned with the Crystal Ball detector on polarised protons and deuterons a specially designed, large horizontal ^{3}He/^{4}He dilution refrigerator was built in cooperation with the Joint Institute for Nuclear Research (JINR) Dubna (see Figure 9). It has minimum limitations for the particle detection and fits into the central core of the inner Particle Identification Detector (PID2). This was achieved by using the frozen spin technique with the new concept of placing a thin superconducting holding coil inside the polarisation refrigerator. Longitudinal and transverse polarisations will be possible.

Highest nucleon polarisation in solid-state target materials is obtained by a microwave pumping process, known as 'Dynamic Nucleon Polarisation' (DNP). This process is applicable to any nucleus with spin and has already been used in different experiments with polarised proton and deuteron targets. The geometric configuration of the target is the same for the polarised proton and neutron setup. However, since the polarisation measurement of the deuteron is more delicate due to the small size of the polarisation signals,

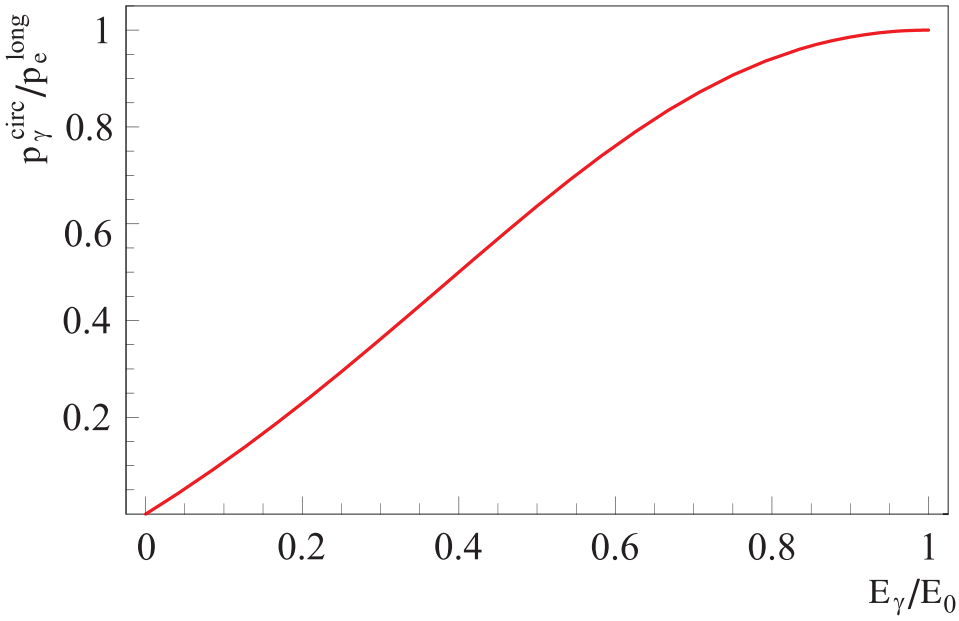

Figure 7: Helicity transfer from the electron to the photon beam as function of the energy transfer. The MAMI beam polarisation is $P_e \approx 85\%$.

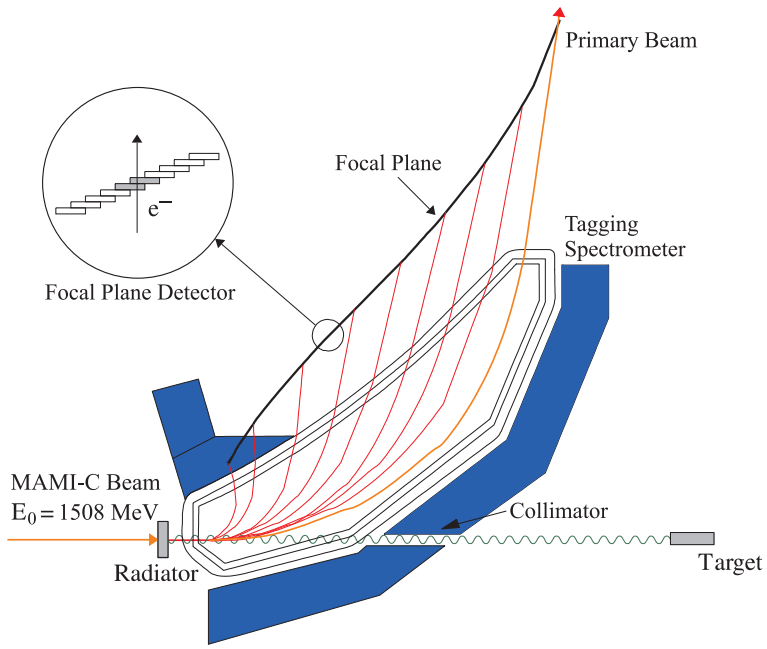

Figure 8: The Glasgow photon tagging spectrometer.

Figure 9: The new dilution refrigerator for the Crystal Ball Frozen Spin Target.

the modification of some basic components is needed. The reason for this is twofold: firstly the magnetic moment of the deuteron is smaller than that of the proton and, in addition, the interaction of the deuteron quadrupole moment with the electric field gradient in the sample broadens the deuteron polarisation signal. An accuracy $\delta P_p/P_p$ of 2 to 3% for the protons and $\delta P_D/P_D$ of 4 to 5% for the deuterons is expected in the polarisation measurement. It has also to be taken into account that the measured deuteron polarisation P_D is not equal to the neutron polarisation P_n. Assuming a 6 % admixture of the D-state of the deuteron, a calculation based on the Clebsch-Gordon coefficients leads to $P_n = 0.91\ P_D$. Several polarised proton and deuteron materials are available such as alcohols and deuterated alcohols (e.g., butanol C_4H_9OH), NH_3, ND_3 or ^{6}LiD. The most important criteria in the choice of material suitable for particle physics experiments are the degree of polarisation P and the ratio k of free polarisable nucleons to the total number of nucleons. Further requirements on polarised target materials are a short polarisation build-up time and a simple, reproducible target preparation. The polarisation resistance against radiation damage is not an issue for experiments with a low intensity tagged photon beam ($\dot{N}_\gamma \approx 5 \cdot 10^7\ \mathrm{s}^{-1}$) as will be used here. However, the limitations of a reduced relaxation time due to overheating of the target beads (Kapitza resistance) will have to be investigated.

Taking all properties together, butanol and deuterated butanol are the best material for this experiment. For protons we expect a maximum polarisation of $P_p = 90\%$ and an average polarisation of $P_p = 70\%$ in the frozen spin mode. Recently, a deuteron polarisation $P_D = 80\%$ was obtained with Trityl doped butanol targets at 2.5 T magnetic field in a ^{3}He/^{4}He dilution refrigerator. At a 0.4 T holding field an average neutron polarisation P_n (see above) of 50 % will be obtained. The filling factor for the $\sim$2 mm diameter butanol spheres into the 2 cm long, 2 cm diameter target container will be around 60%. The experience from the GDH runs in 1998 [22] shows that, with a total tagged photon flux of $5 \cdot 10^7$, relaxation times of about 200 hours can be expected. The polarisation has to be refreshed by microwave pumping every two days.

In conclusion, we estimate that we will achieve the following target parameters:

- Maximum total tagged photon flux in the energy range of 4.7 to 93% of E_0: $\dot{N}_\gamma \approx 5 \cdot 10^7\ \mathrm{s}^{-1}$, with relaxation time of 200 hours.
- Target proton density in 2 cm cell: $N_T \approx 9.1 \cdot 10^{22}\mathrm{cm}^{-2}$ (including dilution and filling factors)
- Average proton polarisation $P_p = 70\%$
- Target deuteron density in 2cm cell: $N_T \approx 9.4 \cdot 10^{22}\mathrm{cm}^{-2}$ (including dilution and filling factors)
- Average neutron polarisation $P_n = 50\%$

A.3 Crystal Ball Detector System

The central detector system consists of the Crystal Ball calorimeter combined with a barrel of scintillation counters for particle identification and two coaxial multiwire proportional counters for charged particle tracking. This central system provides position, energy and timing information for both charged and neutral particles in the region between 21° and 159° in the polar angle (θ) and over almost the full azimuthal (ϕ) range. At forward angles, less than 21°, reaction products are detected in the TAPS forward wall. The full, almost hermetic, detector system is shown schematically in Figure 10 and the measured two-photon invariant mass spectrum is shown in Figure 11.

The Crystal Ball detector (CB) is a highly segmented 672-element NaI(Tl), self triggering photon spectrometer constructed at SLAC in the 1970's. Each element is a truncated triangular pyramid, 41 cm (15.7 radiation lengths) long. The Crystal Ball has an energy resolution of $\Delta E/E = 0.020 \cdot E[GeV]^{0.36}$, angular resolutions of $\sigma_\theta = 2 \ldots 3°$ and $\sigma_\phi = \sigma_\theta / \sin\theta$ for electromagnetic showers [18]. The readout electronics for the Crystal Ball were completely renewed in 2003, and it now is fully equipped with SADCs which allow for the full sampling of pulse-shape element by element. In normal operation, the onboard summing capacity of these ADCs is used to enable dynamic pedestal subtraction and the provision of pedestal, signal and tail values for each element event-by-event. Each CB element is also newly equipped with multi-hit CATCH TDCs. The readout of the CB is effected in such a way as to allow for flexible triggering algorithms. There is an analogue sum of all ADCs, allowing for a total energy trigger, and also an OR of groups of sixteen

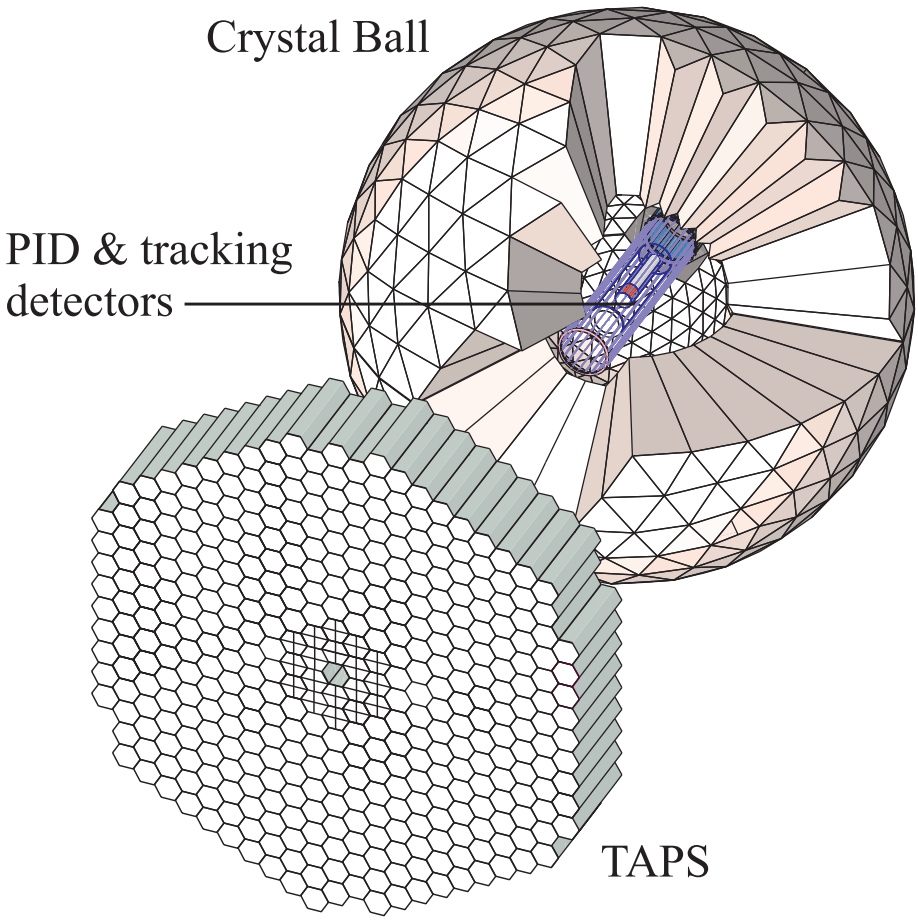

Figure 10: The A2 detector setup: The Crystal Ball calorimeter, with cut-away section showing the inner detectors, and the TAPS forward wall.

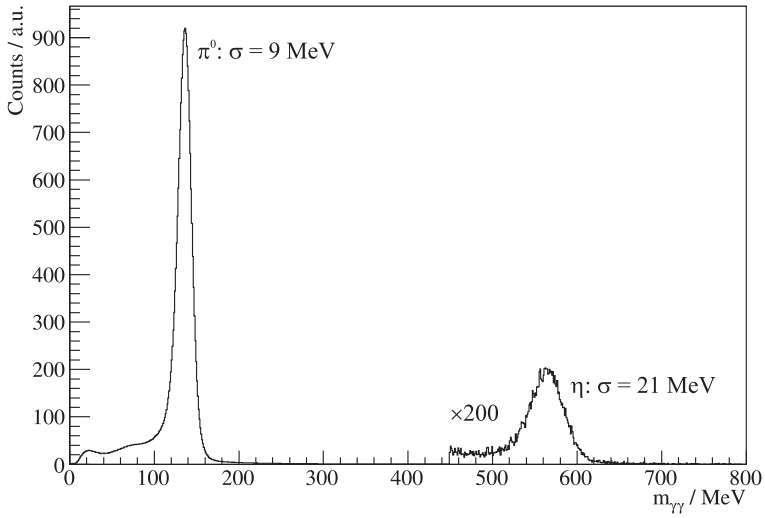

Figure 11: Two photon invariant mass spectrum for the CB/TAPS detector setup. Both η and π^0 mesons can be clearly seen.

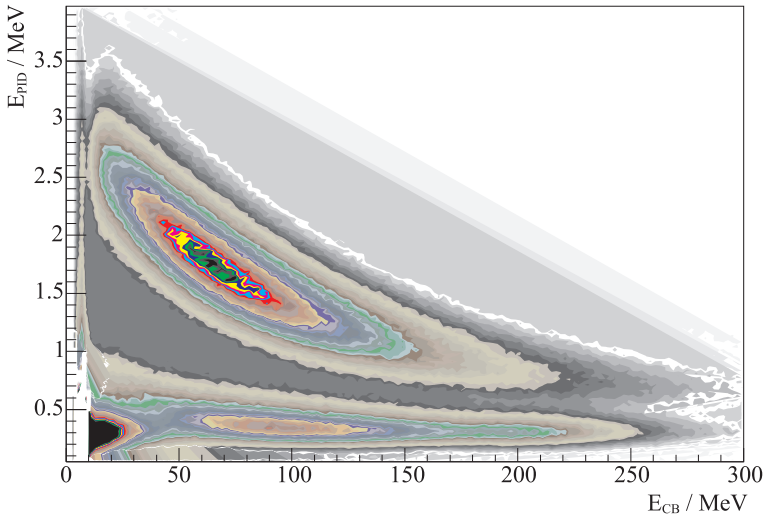

Figure 12: A typical $\Delta E/E$ plot from the Crystal Ball and the PID2 detector. The upper curved region is the proton locus, the lower region contains the pions and the peak towards the origin contains mostly electrons.

crystals to allow for a hit-multiplicity second-level trigger—ideal for use when searching for high multiplicity final states.

In order to distinguish between neutral and charged particles species detected by the Crystal Ball, the system is equipped with PID2, a barrel detector of twenty-four 50 mm long, 4 mm thick scintillators, arranged so that each PID2 scintillator subtends an angle of 15° in ϕ. By matching a hit in the PID2 with a corresponding hit in the CB, it is possible to use the locus of the $\Delta E, E$ combination to identify the particle species (Figure 12). This is primarily used for the separation of charged pions, electrons and protons. The PID2 covers from 15° to 159° in θ.

The excellent CB position resolution for photons stems from the fact that a given photon triggers several crystals and the energy-weighted mean of their positions locates the photon position to better than the crystal pitch. For charged particles which deposit their energy over only one or two crystals, this is not so precise. Here the tracks of charged particles emitted within the angular and momentum acceptance of the CB detector will be reconstructed from the coordinates of point of intersections of the tracks with two coaxial cylindrical multiwire proportional chambers (MWPCs) with cathode strip readout. These MWPCs are similar to those installed inside the CB during the first round of MAMI-B runs [20]. The most significant

difference is that all detector signals are taken at the upstream end of the MWPCs, minimising the material required and facilitating particle detection in the forward polar region.

A mixture of argon (79.5%), ethane (30%) and freon-CF_4 (0.5%) is used as the filling gas. This mixture is a compromise between charge multiplication and localization requirements imposed by the ionizing particle tracks.

Within each chamber both the azimuthal and the longitudinal coordinates of the avalanche will be evaluated from the centroid of the charge distribution induced on the cathode strips. The location of the hit wires(s) will be used to resolve ambiguities which arise from the fact that each pair of inner and outer strip cross each other twice. The expected angular resolution (rms) will be $\sim 2^\circ$ in the polar emission angle θ and $\sim 3^\circ$ in the azimuthal emission angle ϕ.

The MWPCs have been recently installed inside the CB frame and their calibration using both cosmic rays and test beam data is currently underway.

A.4 TAPS Forward Wall

The TAPS forward wall is composed of 384 BaF_2 elements, each 25 cm in length (12 radiation lengths) and hexagonal in cross section, with a diameter of 59 mm. The front of every TAPS element is covered by a 5 mm thick plastic veto scintillator. The single counter time resolution is $\sigma_t = 0.2$ ns, the energy resolution can be described by $\Delta E/E = 0.018 + 0.008/E[GeV]^{0.5}$ [18]. The angular resolution in the polar angle is better than 1°, and in the azimuthal angle it improves with increasing θ, being always better than $1/R$ radian, where R is the distance in centimeters from the central point of the TAPS wall surface to the point on the surface where the particle trajectory meets the detector. The TAPS readout was custom built for the beginning of the CB@MAMI program and is effected in such a way as to allow particle identification by Pulse Shape Analysis (PSA), Time Of Flight (TOF) and $\Delta E/E$ methods (using the energy deposit in the plastic scintillator to give ΔE). TAPS can also contribute to the CB multiplicity trigger and is currrently divided into upto six sectors for this purpose. The 2 inner rings of 18 BaF_2 elements have been replaced recently by 72 $PbWO_4$ crystals each 20 cm in length (22 radiation lengths). The higher granularity improves the rate capability as well as the angular resolution. The crystals are operated at room temperature. The energy resolution for photons is similar to BaF_2 under these conditions [23].

References

[1] R.P. Hildebrant, H.W. Grießhammer, and T.R. Hemmert, Eur. Phys. J. A **20**, 329 (2004).

[2] B. Pasquini, D. Drechsel, and M. Vanderhaeghen, Phys. Rev. C **76**, 015203 (2007).

[3] R.P. Hildebrant *et al.*, Eur. Phys. J. A **20**, 293 (2004).

[4] D. Drechsel, B. Pasquini, and M. Vanderhaeghen, Phys. Rept. **378**, 99 (2003).

[5] D. Drechsel *et al.*, Phys. Rev. C **61**, 015204 (1999).

[6] D. Babusci *et al.*, Phys. Rev. C **58**, 1013 (1998).

[7] G. Gellas, T. Hemmert, and Ulf-G. Meißner, Phys. Rev. Lett. **85**, 14 (2000).

[8] K.B. Vijaya Kumar, J.A. McGovern, M.C. Birse, Phys. Lett. B **479**, 167 (2000).

[9] D. Djukanovic, Ph.D. Thesis, University of Mainz, 2008.

[10] B. Holstein, D. Drechsel, B. Pasquini, and M. Vanderhaeghen, Phys. Rev. C **61**, 034316 (2000).

[11] S. Kondratyuk and O. Scholten, Phys. Rev. C **64**, 024005 (2001).

[12] W. Detmold *et al.*, Phys. Rev. D **73**, 114505 (2006).

[13] J. Ahrens *et al.*, Phys. Rev. Lett. **87**, 022033 (2001).

[14] M. Schumacher, Prog. Part. Nucl. Phys. **55**, 567 (2005).

[15] R. Miskimen, private communication.

[16] B. Pasquini, private communication.

[17] H. Olsen and L.C. Maximon, Phys. Rev. **114**, 887 (1959).

[18] S. Prakhov *et al.*, Phys. Rev. C **79**, 035204 (2009).

[19] J.C. McGeorge *et al.*, Eur. Phys. J. A **37**, 129 (2008).

[20] G. Audit *et al.*, Nucl. Instr. Meth. A **301**, 473 (1991).

[21] A. Reiter *et al.*, Eur. Phys. J. A **30**, 461 (2006).

[22] A. Thomas *et al.*, Nucl. Phys. B **79**, 591 (1999).

[23] R. Novotny *et al.*: Nucl. Instrum. Meth. A **486**, 131 (2002).